Additive Manufacturing 25 (2019) 19–31

Contents lists available at ScienceDirect

Additive Manufacturing

journal homepage: www.elsevier.com/locate/addma

Plastic anisotropy of additively manufactured maraging steel: Influence of the build orientation and heat treatments

Barry Mooney[a], Kyriakos I. Kourousis[a,*], Ramesh Raghavendra[b]

[a] School of Engineering, University of Limerick, V94 T9PX, Ireland
[b] South Eastern Applied Materials Research Centre (SEAM), Waterford Institute of Technology, X91 TX03, Ireland

ARTICLE INFO

Keywords:
Additive manufacturing
3D printing
Maraging steel
Anisotropy
Heat treatment
Strength
Ductility

ABSTRACT

This experimental study investigates the combined effect of the three primary Additive Manufacturing (AM) build orientations (0°, 45°, and 90°) and an extensive array of heat treatment plans on the plastic anisotropy of maraging steel 300 (MS1) fabricated on the EOSINT M280 Direct Metal Laser Sintering (DMLS) system. The alloy's microstructure, hardness, tensile properties and plastic strain behaviour have been examined for various strengthening heat-treatment plans to assess the influence of the time and temperature combinations on plastic anisotropy and mechanical properties (e.g. strength, ductility). A comprehensive visual representation of the material's overall mechanical properties, for all three AM build orientations, against the various heat treatment plans is offered through time – temperature contour maps. Considerable plastic anisotropy has been confirmed in the as-built condition, which can be reduced by aging heat-treatment, as verified in this study. However, it has identified that a degree of transverse strain anisotropy is likely to remain due to the AM alloy's fabrication history, a finding that has not been previously reported in the literature. Moreover, the heat treatment plan (6h at 490 °C) recommended by the DMLS system manufacturer has been found not to be the optimal in terms of achieving high strength, hardness, ductility and low anisotropy for the MS1 material. With the use of the comprehensive experimental data collected and analysed in this study, and presented in the constructed contour maps, the alloy's heat treatment parameters (time, temperature) can be tailored to meet the desired strength/ductility/anisotropy design requirements, either for research or part production purposes.

1. Introduction

Structure-critical metallic components, produced by additive manufacturing (AM), are expected to display a high degree of isotropy. The dependence of mechanical properties on orientation, known as *anisotropy*, is a consequence of the metal's fabrication history which places limitations on the design of the part. Maraging steels possess the mechanical properties which give them engineering significance in applications where high-strength, toughness and ductility (at high-hardness), and dimensional stability are required [1–3]. Based on the binary Fe-Ni primary phase system, the highly-alloyed steel is strengthened by finely dispersed precipitates, which block movement of dislocations/defects within the crystal lattice. The dispersion of secondary phase alloying elements (Mo, Co, Ti and Al), mobilized through a straightforward and relatively expeditious aging heat-treatment, leads to an exceptional combination of strength and toughness [4–6,2]. Maraging steel's low-carbon soft martensitic matrix is mostly free from interstitial alloying elements, which rank it as an excellent candidate for synthesis by AM and welding [1,6–8]. The 18Ni (300) grade,[1] or slight modifications thereof, has been used in AM, and is retailed commercially in powder form under several aliases. The quality assured *MS1* is one such powder supplied by EOS [10]. This powder has been suitably refined for EOS's powder-bed AM systems and processing techniques, which have retained the historical proprietary name *Direct Metal Laser Sintering* (DMLS). Another, commonly used, term for this process is Selective Laser Melting (SLM), since the technique employs a high-powered laser-beam energy source to fully melt powder particles into a high density, and chemically homogeneous composition. Driven by computer aided design (CAD) data, the laser's scanning strategies can be used to achieve layer-wise growth of imaginative, and relatively unconstrained geometries [11,10].

It is the alloy's outstanding properties and heat-treatment

* Corresponding author.
E-mail address: Kyriakos.Kourousis@ul.ie (K.I. Kourousis).

[1] One of the four commercial maraging steel grades developed by Inco, where each grade was optimised in terms of strength and toughness. The *300* designation represents the grade's yield strength in ksi units [9]

https://doi.org/10.1016/j.addma.2018.10.032
Received 31 July 2018; Received in revised form 3 September 2018; Accepted 18 October 2018
Available online 31 October 2018

expediency in conjunction with the AM process's shaping efficiency that give DMLS produced maraging steel 300 such appeal. These factors allow for a much-accelerated fabrication route than conventionally manufactured (CM) parts, and thus offsets the high acquisition cost of the alloy, as well as the process costs. DMLS built maraging steel 300, however, has a major drawback amongst its CM counterpart. The mechanical properties are known to be anisotropic due to an inherent sensitivity with regards to how a part is orientated within the AM build volume [11–13]. This anisotropy is manifested through the fabrication process where large thermal gradients during melt-pool solidification, combined with the layer-wise deposition of the powder, planar movement of the heat source, and uniaxial movement of the build-plate, make it difficult to homogenize the microstructure and mechanical properties of the as-built metal. A mesostructure of fine solidification cells, unique to the powder processing method and consequent to the powder granule melt dynamics, is coupled with continuous re-melting/ heating of material beneath the melt-pool during build-up causes a distinct three-dimensional (3D) microstructural pattern to form. This results in mechanical properties which vary with direction and causes the material to exhibit anisotropic mechanical properties. Furthermore, the state of anisotropy can be exacerbated by ancillary process defects, such as residual stresses, and porosity, and a number researchers have investigated the effect of AM processing parameters to improve the build quality of maraging steel 300 [14–16].

As indicated by EOS in the MS1 material data sheet (MDS) [11], the material becomes isotropic following application of a specified aging heat-treatment (6h at 490 °C), however, the MDS is not sufficient to characterize the material performance for engineering designs and products, since it covers only the primary build orientations (0°, 90°), and comes from a single source (EOS). The effectiveness of both the AM fabrication and heat-treatment procedure can only be measured by the extent to which the as-built and treated component behaves under mechanical loading, yet very limited published research [17,18] exists concerning the build orientation influence on mechanical behaviour of AM-produced maraging steel 300. [18], who investigated the dependence of build orientation relative to the build plane (0°, 45°, and 90°) on the high-cycle fatigue life of EOS M280 produced MS1 specimens in the aged (6h at 490 °C) condition only, found no substantial difference on the fatigue properties. Recently, [17] examined the tensile properties of EOS MS1 fabricated at 0°, 45°, and 90°, and contrary to the EOS published MDS [11] they observed no significant orientation dependence in the tensile stress-strain behaviour for as-built, solution heat-treated (1 h at 820 °C), and aged (6 h at 490 °C) material. Other available test-data is mainly limited to static testing (tensile, and/or hardness) of maraging steel 300 fabricated in one [19,14,7,20,6,21,22,3,23,24], or two [25,26,12,16,27] of the primary AM build orientations. The most comprehensive of these studies in terms of the reported mechanical properties is [7], which monitors the effect of an array of aging heat-treatments on the static properties of AM fabricated maraging steel 300. While the study presents a broad range of hardness results, only very limited tensile properties are reported (i.e. for the as-built and five other peak-aged heat-treatment conditions). Furthermore, only the horizontal (0°) build-orientation is considered. Authors [28,29] and [16] also present hardness and tensile data for horizontal specimens tested under a narrow array of aging treatments. In these studies, however, non-characteristic fluctuations/ variations in the AM alloy's elasticity and plasticity behaviour can be observed. While explanations for these abnormalities are not asserted, they may indeed be introduced during the fabrication process and/or during the material characterization process (e.g. due to the tensile test rates employed). Nevertheless, these irregularities mandate a more comprehensive and detailed experimental analysis of AM maraging steel 300 monotonic behaviour. So far, the effect of aging heat-treatment on stress and strain anisotropy for this particular material has not been previously addressed, and there have been no reported findings on strain anisotropy for parts fabricated at various build orientations (i.e. 0°, 45°, and 90°). Moreover, the availability of tensile properties for AM fabricated maraging steel 300 for the primary build orientations (0°, and 90°) is limited. Other significant work has been performed to-date in characterizing the microstructure [23,30,31,29,27,32], precipitation reactions [33,6], and austenite reversion behaviours [34,21,7,30] with several of these studies reporting similar microstructures in maraging steel 300 having been produced on a range of AM machines under varying process parameters.

Since it is necessary to consider the material's multiaxial mechanical properties during the process of mechanical component design, the lack of orientation dependence data presents challenges for engineers when it comes to utilising the highly advantageous AM technology for their engineering designs and products. In order to address the aforementioned research literature gaps, in this work, we report a comprehensive experimental analysis of maraging steel 300 mechanical properties and plastic anisotropy behaviour. In doing so, we take into account both the effect of three AM build-orientations (0°, 45°, and 90°), as well as a large array of heat-treatment plans (combinations of time, and temperature) to allow for a wide-scale investigation of anisotropic variation, not previously conducted in the past for this AM material. Plastic anisotropy describes an uneven response of the alloy's plastic properties (or flow-strain relationships) with respect to the AM build orientations, and has been quantified in this investigation by the *R-value* parameter. R-value is the ratio of true width-to-thickness plastic strains, and this parameters allows an examination of the alloy's tendency to strain non-uniformly by consequence of the test-coupon's build-orientation. The full mapping of AM fabricated maraging steel 300 mechanical properties for all three build orientations, in conjunction with their respective R-values has not previously been reported in the literature, and can serve as a very practical tool for AM engineers and researches wishing to tailor the output of the EOS MS1. This novel experimental work is particularly focused on providing a means of AM maraging steel 300 heat-treatment selection to meet individual strength/ ductility/ anisotropy engineering design requirements, and intends to act as a guide project for other AM manufactured metals exhibiting anisotropy.

2. Material and methods

2.1. Material and AM process

Gas-atomized MS1 powder feedstock supplied by EOS was used. The chemical composition of the raw-material is shown in Table 1, which corresponds to US classification 18 Maraging (300), German X3NiCoMoTi 18-9-5, and European 1.2709 [35]. In the same table, the results of the energy dispersive x-ray (EDX) analysis, conducted with a Hitachi SU 70 Scanning Electron Microscope (SEM), for the main comprising elements are also presented. The powder presented spherical particles typically measuring under 50 µm. The SEM morphology and particle

Table 1
Chemical composition (%wt) of MS1, the 18Ni (300) grade maraging steel powder supplied by EOS [11] with SEM-EDX analysis results for the main comprising elements (EDX sampling area: ≈10µm^2).

	Ni	Mo	Co	Ti	Al	Cr	Si	Mn	C	Fe
MS1 [11]	17–19	4.5–5.2	8.5–9.5	0.6–0.8	0.05–0.15	0–0.5	0–0.1	0–0.1	0–0.03	Bal.
SEM-EDX	18.14	5.67	8.94	0.87	-	-	-	-	-	Bal.

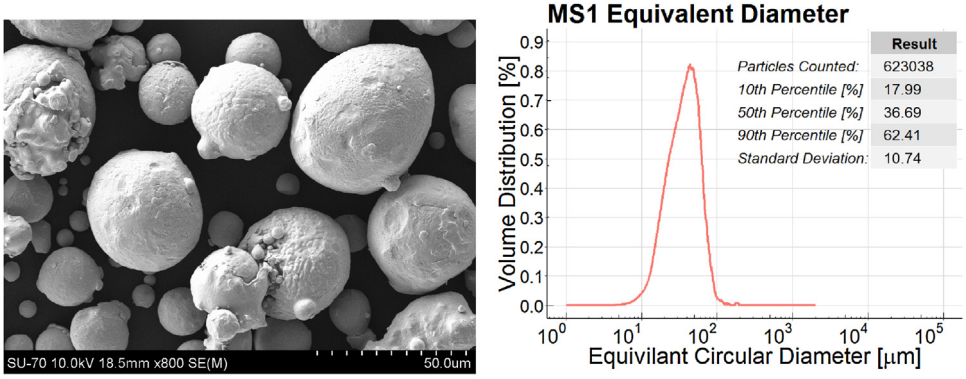

Fig. 1. (a) SEM morphology of the MS1 powder, and (b) powder particle size distribution (circular equivalent diameter) with statistical details inset.

size distribution, analysed using a *Malvern Morphologi G3* particle analyser, are shown in Fig. 1(a) and (b) respectfully. The observed median particle size was 36.69 µm, and had a standard deviation (SD) of 10.74 µm. The median particle circularity (deviation from a perfect circle, where perfect circularity = 1) was 0.956.

A rectangular-shaped tensile test specimen, meeting the requirements of the ASTM E8M standard [36], was selected to allow for both lateral and axial elastic and plastic strain measurements whilst under tensile loading. The test specimen geometry, dimensions and tolerances are shown in Fig. 2(a). Test-specimens having a uniform cross-section at gage, were fabricated at SEAM, IE using the EOS *EOSINT M280* system within an atmosphere of inert Nitrogen over the course of three consecutive AM builds. The M280 was equipped with 200W Ytterbium-fibre laser and was fitted with the manufacturers recommended (for MS1) ceramic re-coater blade. To investigate the influence of build orientation on property anisotropy, test-specimens were fabricated in the Y-Z build plane at three angles (0° (horizontal), 45° (inclined), and 90° (vertical)) between their longitudinal axis and the build platform, as shown in Fig. 2(b). A total of forty-eight (48) samples were fabricated (i.e. sixteen (16) test-pieces for each AM orientation) from a virgin batch of MS1 feedstock over three consecutive AM builds.

As shown in Fig. 3, the AM build leaves visible ridges upon parts' build surfaces and a stair-stepped effect on 45° sloping surfaces which are indicative of the layered fabrication process. High roughness at the surface can augment crack initiation thus leading to pre-mature failure. Furthermore, these ridges hinder the accurate evaluation of gage width and thickness dimensions. Ductility calculations are sensitive to the measurement of gage cross-sectional area, while the ASTM E8M standard exhorts that particular attention be given to the uniformity and quality of surface-finish with regards high-strength specimens [36]. For these reasons, an additional 0.5 mm of machinable material was added to each face prior to the AM-build. This surplus material, which was later machined by single-cycle precision computer numerically controlled (CNC) wire electrical discharge machining (EDM) profiling and surface-grinding operations, had the extra benefit of safeguarding against potential thermally induced distortion.

The EOS M280 machine's hardware was driven by the factory default, undisclosed, and pre-optimized set of parameters *'MS1 Performance 2.0'* which has been developed by the manufacturer for this specific material and machine combination [35]. EOS claims that their set of parameters (*MS1 Performance 2.0*) ensures reliable mechanical properties. This offers a defined part property profile bolstering industry-level repeatability and quality [37]. A vertical support-scaffold connected the under-side of each specimen to the manufacturer's recommended building platform (Steel 1.2083 36mm thick DirectBase TS36P) [35]. This structure played two important roles during the elevated temperature production cycle - (a) it functioned as a passive heat-sink during manufacturing; and (b) it reinforced the 45° inclined specimens against cross-platform re-coater forces and earthward gravitational forces. As verified by the post-build inspection, the process had achieved sound metallurgical bonding between layers, with a uniform and characteristic ridged surface. The parts were dimensionally accurate, however it is worth noting that a longitudinal shrinkage distortion (bowing) in the AM build direction (*Z*), to the extent of ≤ 0.1 mm, was observed in several horizontal (0°) specimens after their removal from the build-plate. This shrinkage, which was rectified in the downstream machining operation, is understood to have been brought about by a build-up of thermal stresses developed between the raw-material and base-plate metal during the heating and cooling cycles over the opening number of layers.

The heat treatment (aging) was performed in a pre-heated Elite Thermal Systems 120 litre 6kW heavy duty-fan oven (air atmosphere)

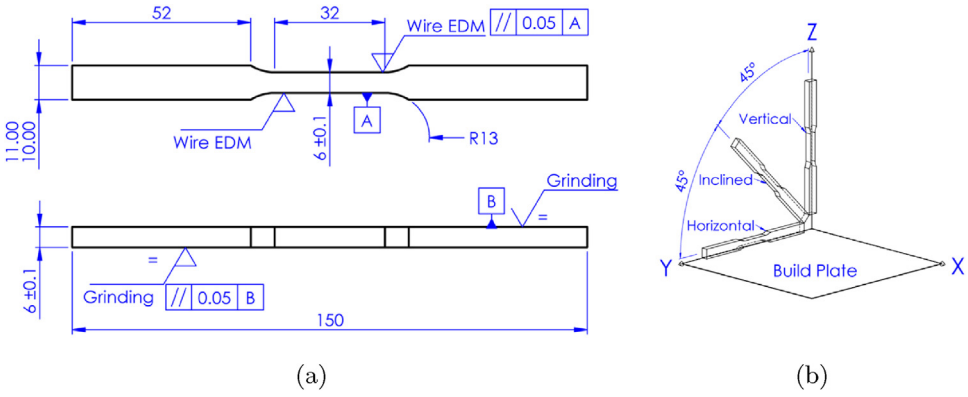

Fig. 2. (a) Showing the finish-machined specimen geometry, and (b) the AM build volume coordinate system and test-specimen build orientations.

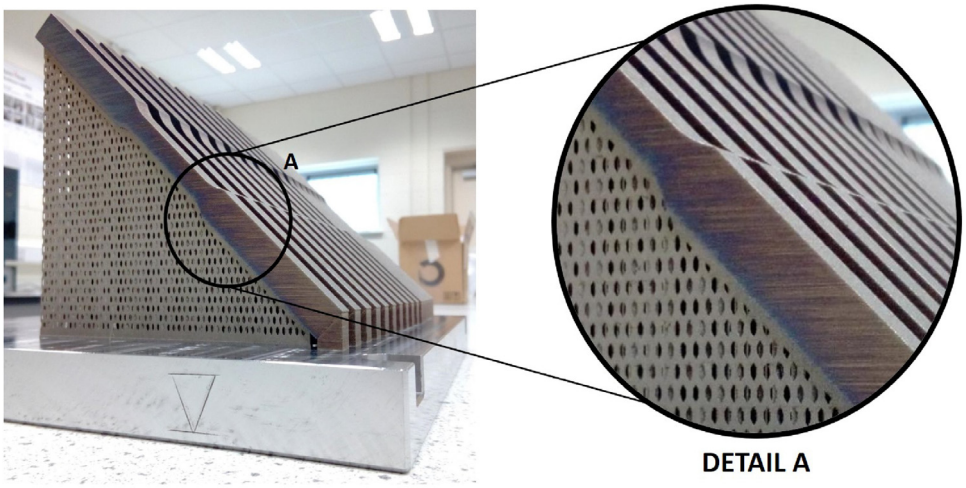

Fig. 3. DMLS fabricated samples of the 45° build orientation before detachment of the support scaffold from the parts/build-platform. Detail A highlights the presence of distinct surface ridges which are consequent to the layer-wise fabrication process.

Table 2
Showing the experimental heat-treatments applied to full-sets of test-specimens (i.e. 0°, 45°, 90°), where the characters *'T'* and *'H'* symbolize a tensile, and/or Vickers Hardness test-campaign.

Temperature	Aging time [hours,h]										
[°C]	1 h	2 h	3 h	4 h	5 h	6 h	8 h	10 h	12 h	15 h	16 h
460 °C	-	-	-	-	H	T,H	T,H	H	T,H	-	H
490 °C	-	-	H	-	H	T,H	-	-	H	-	-
525 °C	-	-	H	T,H	H	T,H	T,H	H	-	H	-
540 °C	-	H	-	T,H	H	T,H	T,H	H	-	-	-
600 °C	T,H	T,H	H	T,H	H	T,H	H	-	-	-	-

controlled by dual Eurotherm 3216 PID temperature controllers and cooled slowly in still air at ambient temperature (23°*C*). The experimental heat-treatment plan is shown in Table 2, where T denotes tensile tests and H the Vickers hardness measurements performed for a set of 0°, 45°, 90° specimens.

The treatment temperature dictates the kinetics of phase separation in the alloy's matrix, and ultimately determines the population and size of precipitates which form, thus, aging temperature has the most significant effect on precipitate size and dispersion in maraging steels [38]. The EOS recommended heat-treatment temperature of 490 °*C* allows a populous dispersion of hindering precipitates to form over the stated 6h aging period. It is the interaction between dislocations and precipitates which determines the material's strength and ductility. Prolonged holding at temperatures below austenite start ($A_s \approx 560$ °C) not only reduces the effectiveness of dislocation hindrance but will eventually lead to a decomposition of martensite by diffusion-controlled reactions to a stable blend of austenite and ferrite. Aging at temperatures approaching A_s reduces the population of developing precipitate particles and heightens the propensity for austenite reversion where its formation can even precede precipitation. Higher aging temperatures are employed when good toughness/ductility is sought, and to that end - the EOS M280 parameter sheet [39] outlines an aging treatment of 6 h at 525 °C (−600 °C). The experimental heat-treatments (Table 2) were therefore selected to confirm EOS recommendations; to formulate a comprehensive evaluation of static mechanical properties; and to allow for wide-scale investigation of the anisotropy variation.

2.2. Characterization

A Taylor Hobson *Hommel Tester T500* surface profiler was used to measure the roughness variation due to surface orientation within the build volume. For each build orientation, the profiler's stylus was traced along specimens' loading axis using an assessment length of 4.8 mm. Two roughness parameters were utilised:

- *Rz* representing the mean roughness depth by calculating the average value of the five highest peaks and five deepest valleys over the assessment length;
- *Ra* corresponding to the arithmetical mean surface roughness value of all profile deviations over the assessment length.

Archimedes' Principle density measurements, in compliance with ASTM B962-17 [40], were performed using a *Sartorius Quintix* laboratory balance (model 65-1S) equipped with accessory YDK03 density determination kit.

Uniaxial tensile tests were conducted at ambient temperature in a calibrated *Zwick/Roell (Dartec) M1000/RK* servo-hydraulic closed-loop testing machine equipped with 100 kN capacity load cell and fitted with ± 100kN fatigue rated hydraulic wedge grips. The test routine followed strict adherence to the guidelines present in ASTM E8M [36]. The test was initially controlled (via 9600 series controller) to the elastic stressing rate of 10.34 MPa/s, using strain control from the extension feedback channel (Epsilon model 3542-025M-050-ST). Upon detection of yield, the test-rate maintained a constant plastic strain rate of 6.25×10^{-4}/s controlled via the stroke feedback channel. At the end of the yield (detected from either reaching a 5% increase in stress, or an absolute strain limit of 2%), the test-velocity was commanded by a third rate, the tensile strength (R_m) rate: 0.0068/s. This strain rate was maintained to peak force, and through to failure.

Non-contact full-field strain and deformation was measured and analysed using *La Vision's* portable 3D Digital Image Correlation (DIC) apparatus. The apparatus comprised of (i) two 12-bit Imager E-lite CCD-chipped cameras fitted with 35 mm lenses, (ii) two gated white light sources each containing twelve linear-configured LEDs, (iii) a *StrainMaster* Controller and data-acquisition unit with integrated analogue-to-digital converter (A/D), and (iv) a dedicated PC complete with *StrainMaster®* processing software. The experimental arrangement is shown in Fig. 4. Each camera was focussed onto the measurement plane providing an overlap region upon the specimen gage surface. The enclosed angle between cameras and the working distance between each camera and the test-specimen was ≈20° and ≈350 mm respectively. Using the stereoscopic camera system's in-situ position, a global 3D-coordinate system was derived by means of a precursory calibration step involving a 3D two-level calibration target/plate. This included the generation of a fit mapping function with the calibration plate from

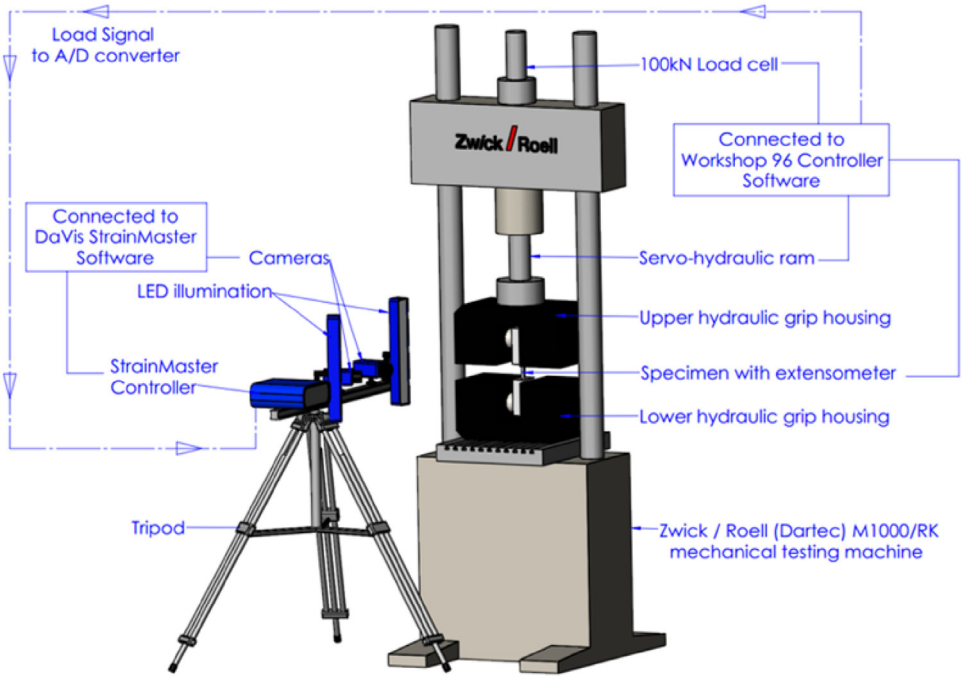

Fig. 4. Configuration of tensile test set-up including the 3D Digital Image Correlation (DIC) apparatus which allowed concurrent determination of test-specimen width and axial strains (ε_w and ϵ_l).

which the average deviation of the dewarped calibration target positions to the ideal positions was lower than 0.3 pixel. This corresponds to an excellent fit, and an appropriate basis for the proceeding full-field 3D strain-measurement evaluations [41]. A high-contrast acrylic paint dark 'speckle' pattern (dark black speckles on a bright white background) was applied to the area of interest (i.e. the specimens' gage surface). Special attention was given to achieving a relatively fine pattern scale (for higher spatial resolution) with a non-repeating isotropic distribution. In this study, each subset (or "window") had an area of 37 pixels^2, which translated to approx. 1.75 mm^2. The goal of the speckle is to provide each subset with a unique signature pixel arrangement from which the displacement pattern can be tracked in 3D space with micron accuracy by the StrainMaster software's pattern matching algorithm [42]. A sequence of images was captured during each tensile test (i.e. from zero applied load to fracture) at a periodic rate of 5 Hz. A displacement vector corresponding to each subset was calculated by the StrainMaster least squares matching algorithm from a reference (undeformed) image. The basic result of the DIC analysis was a full-field 3D displacement measurement evaluation containing thousands of measurement points. In accordance with ASTM test methods E132-04 and E517-18 [43,44], Poisson (ν) and plastic strain ratios (R-values) have been evaluated using DIC data. In turn, the individual test-specimen R-values (R_0, R_{45}, and R_{90}), are unified by the parameter ΔR which is used to quantify planar anisotropy (i.e. in the AM Y-Z plane) by Eq. (1).

$$\Delta R = \frac{1}{2}(R_0 - 2R_{45} + R_{90}) \quad (1)$$

Metallographic samples were sectioned and mounted with Buehler Ltd. *PhenoCure* compression mounting compound, and standard finishing steps applied - including polishing with oil based monocrystalline diamond suspension (6μm and 1 μm), *MetaDi* from Buehler Ltd.. Modified Fry's reagent was used to reveal the microstructure which was observed via an *Olympus BX60* Optical light microscope, and *Hitachi SU 70* Scanning Electron Microscope equipped with an *Oxford Instruments EDX attachment* for analysis of the comprising chemical elements.

The progress of the aging heat-treatment was evaluated using a calibrated *Zwick ZHV* Vickers macro-hardness tester and verified with a standard test block to the requirements of ASTM E92-92 [45]. Samples were sectioned, mounted, and polished, then subjected to a 30 kg test force which was applied parallel to the AM material's tensile loading axis (i.e. perpendicular to the sectioned plane). At least 20 hardness measurements were performed on each test specimen, and the results and test statistics were computed using the R statistical software package [46].

The material's crystal structures were qualitatively analysed (for selective heat-treatments) via a *PANalytical Empyrean Pro* multipurpose X-ray diffractometer (XRD) using Cu Kα radiation. Crystallographic phase identification was achieved using HighScore Plus software.

3. Results and discussion

3.1. Surface roughness and density analysis

The as-built and machined surface roughness, along with density (ρ) measurements, are presented in Table 3. The EOS quoted density of 8.0–8.1 g/cm^3, and roughness parameters for as-built horizontal up-facing or vertical (90°) surfaces produced with 40 μm layer-thickness (Rz = 28 μm and Ra = 5 μm) are in general agreement with the presented results. The measurements imply that part density is not influenced by AM build orientation. Regarding chemical composition - there was close agreement between SEM-EDX and the published values [11] for MS1 as shown in Table 1.

Table 3
Axial surface roughness and density measurements (ASTM B962) for the as-built Horizontal (0°), Inclined (45°), and Vertical (90°) MS1 specimens.

	Build Orientation			
	0°	45°	90°	Machined
Rz (μm)	29.21	16.17	21.69	0.47
Ra (μm)	6.63	3.04	4.2	0.09
ρ (g/cm^3)	8.051	8.050	8.049	NA

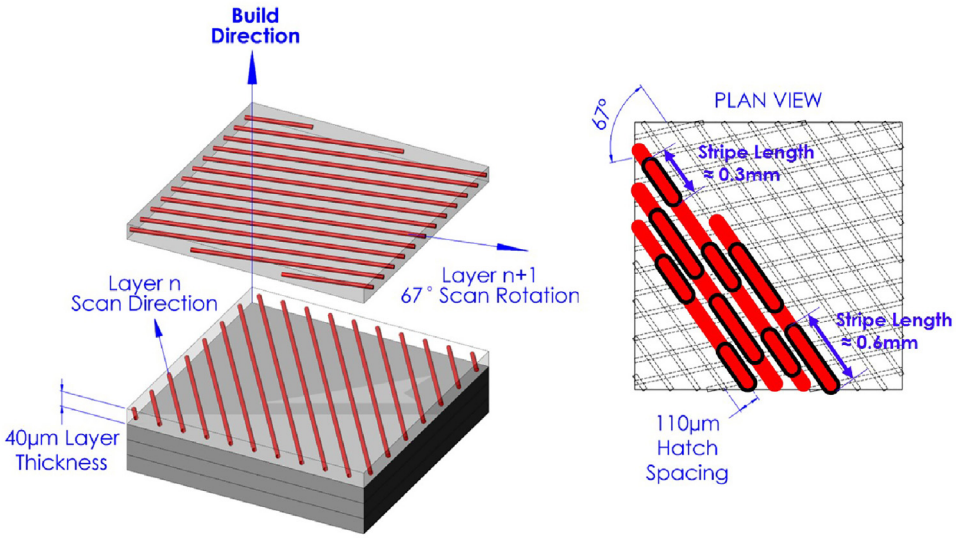

Fig. 5. Schematic representation of the DMLS laser scan strategy which has been inferred from microstructural observations. Each layer's uni-directional line-scan was divided into short stripes of length 0.3–0.6 mm to prevent excessive localized heating.

3.2. As-built microstructure

A schematic representation of the laser scan strategy pertaining to the manufacturer's recommended set of parameters (*MS1 Performance 2.0*) is shown in Fig. 5. This set of parameters prescribed uni-direction line-scans with a laser hatch-spacing of 110 μm. The hatch-spacing and line-scan direction remained constant within each AM layer where each line-scan was segmented into stripe divisions of approximately 0.3–0.6 mm, presumably to prevent excessive localized heat build-up during fabrication. The scan-direction was rotated by 67° for each consecutive 40*μm*-thick layer in an effort to homogenize the microstructure. The outcome is a practically fully dense part, with strong inter-layer and intra-layer metallic bonding. No significant process defects in the form of porosity or un-melted powder particles were observed in the microstructures. It is understood that the absence of defects is largely due to the powder characteristics, since an abundance of small spherical granules in the virgin feedstock augmented flowability and allowed maximum space occupancy during re-coating upon previously distributed layers.

Fig. 6 presents optical macrographs, and as-built SEM micrographs for each build-orientation. The AM characteristic laser melt tracks are apparent at low magnification in Fig. 6(a), (b), and (c). The typical as-built horizontal maraging steel 300 macrostructure (Fig. 6(a)) has a complect appearance, with bundled interconnections of fan-shaped solidification cells between molten lines. The moderately sized melt-pool widths (45–70 μm), and depths (35–55 μm) are reflective of the applied laser energy input (< 200 W). The observed melt-pool width is indicative of a laser focus diameter of ≈ 60μm, while the measured melt-pool depth is typical for this powder layer-thickness (40 μm). Larger laser focus-diameters (100 μm) have been used with higher capacity AM platforms (laser power: 285W) administering equivalent layer-thickness [30]. By contrast to the horizontal cross-section, the 67° rotation of laser scan angle (between the sectioned and preceding layers) is clear on the vertical cross-section (Fig. 6(c)).

As observed in the high-magnification SEM images (Fig. 6(d), (e), and (f)), the AM laser scanning algorithm gives rise to various cellular morphologies including fine, coarse, and dendrite cell formations (highlighted on the images by dotted lines). The evolution mechanisms of these growth formations relate to the melt-region thermal flux direction which changes for successive layers and is theoretically explained in a recent study by Tan et al. [30]. Assisted by rapid cooling rates (circa 10^3 to 10^8 $K.s^{-1}$), these very fine cellular formations orientate themselves concurrent with the direction of heat flow/removal [29,27,26,33,23,34]. Interestingly, other research [27,47] has failed to identify any dominant crystallographic or fibre texture with a preferred grain growth orientation from the AM processed alloy. This suggests that maraging steel 300 may be less susceptible to texture-generated anisotropy than other AM fabricated materials (see [48–51]) which exhibit strong crystallographic preferred orientation. The SEM observed cellular morphology is believed to be a major contributor to the strength difference between AM as-built versus the solution-annealed conventionally produced alloy, which in-contrast does not display retained austenite in its microstructure, and exhibits random parent grains, each containing coarse and disordered packets of parallel lath-martensite [3,6,52,34,16]. Retained austenite is easily distinguishable in the high magnification images (Fig. 6(d), (e), and (f)) as the bright-colour phase which aggregates at cell boundaries. It occurs when the material cools rapidly from austenite finish (A_f) to ambient temperature, essentially freezing in place solute-rich austenite leaving it untransformed, whereas solute depleted austenite transforms into martensite. Accordingly, the importance of appropriate processing variables is evident since these will govern the volume of retained austenite in microstructure, and ultimately the part performance. To-date, however, no studies have quantified the effect of as-built (retained) austenite on the post-heat-treated mechanical properties of AM-fabricated maraging steel 300.

3.3. Aged microstructure

Micrographs of the aged alloy, and their corresponding XRD spectra are presented in Figs. 7, and 8 , to demonstrate the effect of aging temperature on the reversion of metastable bcc martensite phase (Fe-α) to fcc austenite (Fe-γ). The reversion occurs during extended isothermal aging at temperatures which support the dissolution of first-stage metastable Ni_3Mo and Ni_3Ti precipitates ($T > 450$°C). These phases are later replaced with Fe_2Mo and/or Fe_7Mo_6 during a second stage development [26,33][38]. As these new phases nucleate and grow they deplete the matrix of iron, further enhancing the Ni concentration, thus augmenting austenite reversion [53][38]. At higher temperatures these nucleation sites quickly saturate by diffusion of solute elements from the surrounding lattice. This effect combined with early onset of precipitate coarsening (overaging), causes a reduction in the alloys strength capabilities, i.e. a softening behaviour. Lower temperatures control/extend precipitate nucleation and growth, suppress austenite

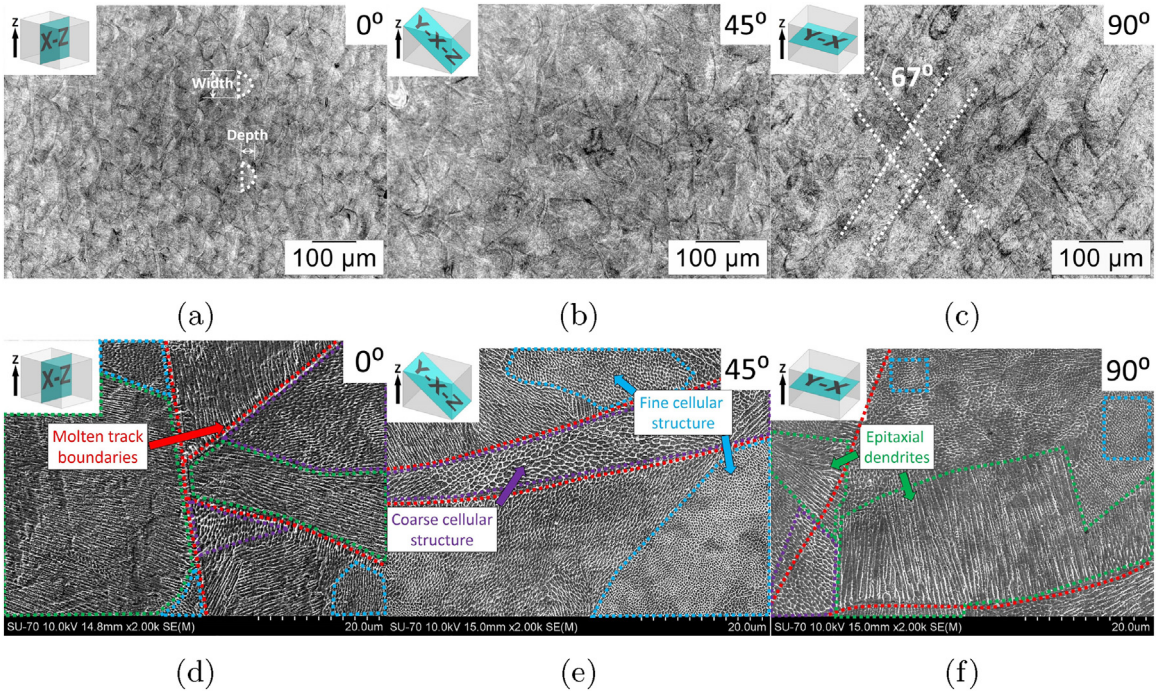

Fig. 6. Representative low magnification (optical) and high magnification as-built (SEM) cross-section images of the MS1 macrostructure/microstructure for three-build orientations: (a) and (d) horizontal (0°); (b) and (e) inclined (45°); and (c) and (f) vertical (90°). The optical images reveal melt-pool solidification patterns, whilst SEM reveals a mesostructure of circular and dendrite cells exhibiting retained austenite at cellular boundaries.

reversion, and allow a populous dispersion of small precipitates [38]. However, it takes considerably longer aging times for these precipitates to reach a stage where dislocation bowing is optimized, corresponding to a given temperature's peak-strength. The milder aging cycle of 6 h at 460 °C presents a microstructure (Fig. 7(a)) comparable in appearance to that of the as-built metal (Fig. 6(d), (e) and (f)). Moreover, there is no noticeable phase change observed in the XRD spectra of as-built and 6h at 460 °C treatments. As observed in Fig. 7, the austenite phase develops markedly at temperatures upwards of 490 °C, where the bright cellular boundaries loose definition, and the volume fraction of the austenite phase readily increases. This is also reflected in the X-ray diffraction data (Fig. 8) where the intensities of Fe-α peaks reduce, and Fe-γ peaks increase with greater aging temperatures.

3.4. Mechanical properties

Vickers hardness aging curves, and a selection of uni-axial Stress (σ) versus Strain (ϵ) curves are presented in Figs. 9, and 10 respectively. Their associated mechanical property values are listed in Table 4. The data convey the extent of mechanical property variation across the as-built build-orientations, and the examined heat-treatments. Despite the seeming closeness among the as-built strength and hardness values, an unusual ductility behaviour occurred in the 45 ° inclined orientation's stress versus strain curve (Fig. 10). In particular, a faster reduction in strength is observed, leading to failure at ≈50% less elongation when

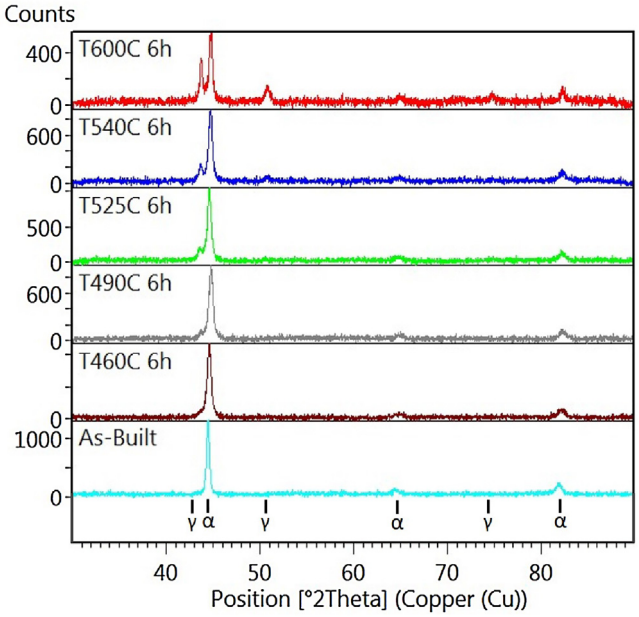

Fig. 8. XRD spectra for DMLS MS1 as a function of aging temperature. The Fe-α and Fe-γ diffraction positions are highlighted on the plot.

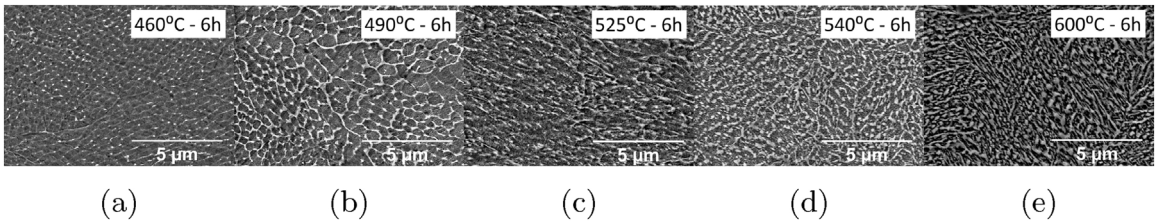

Fig. 7. SEM micrographs of AM maraging steel 300 aged for 6 hours at various temperatures (460, 490, 525, 540, 600 °C) showing a reversion of austenite at solute rich cell boundaries with increased temperature.

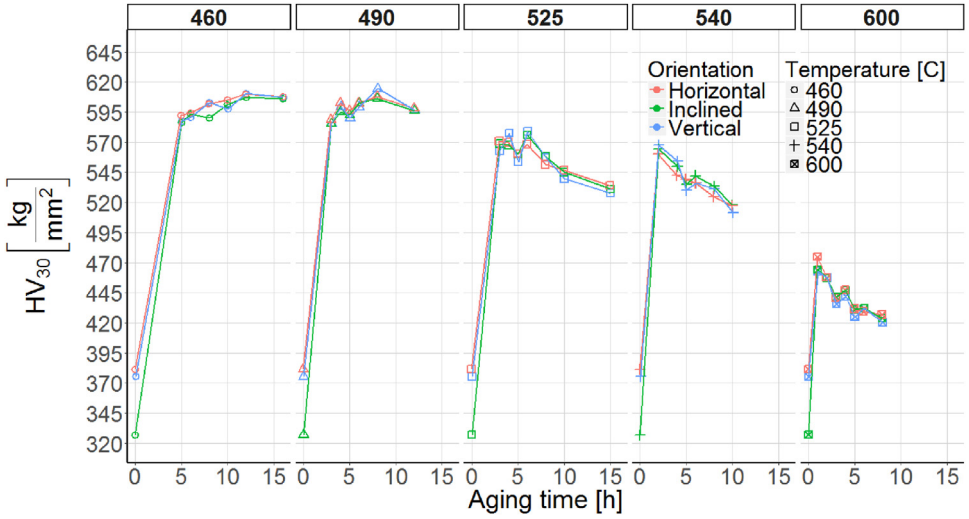

Fig. 9. Precipitation strengthening curves demonstrating the effect of heat-treatment time and temperature parameters on the attainable hardness and anisotropy of AM MS1.

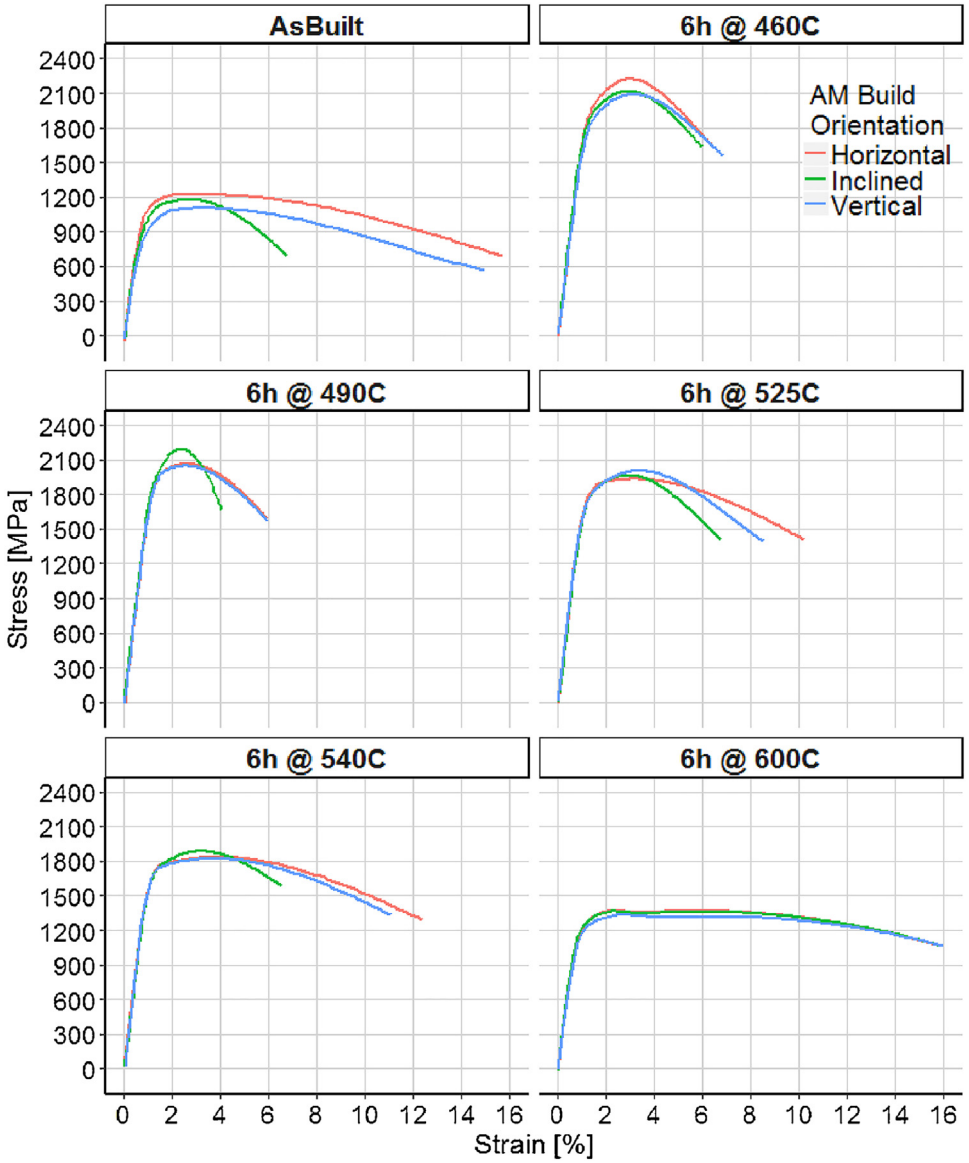

Fig. 10. Excerpt of σ-ϵ curves obtained from the as-built and aged (at 6 h) test-specimens.

Table 4
Mechanical properties data retrieved from tensile and Vickers hardness testing of MS1 produced by DMLS (Elasticity modulus (E); Poisson ratio (ν); Yield strength ($R_{p0.2}$); Tensile strength (R_m); Elongation to fracture (At); Reduction in area (Z); and Vickers hardness (HV)). EOS reference data [11] are shown with italics fonts.

Heat-Treatment	Orien-tation	*E* [GPa]	ν	$R_{p0.2}$ [MPa]	R_m [MPa]	*At* [%]	*Z* [%]	HV_{30kgf} [kg/mm^2]
EOS As-Built[11]	0°	*160* ± 25	-	*1050* ± 100	*1100* ± 100	*10* ± 4	-	*(310-360)*
	90°	*150* ± 20	-	*1000* ± 100	*1100* ± 100	*10* ± 4	-	*(310-360)*
EOS Aged[11]	0°	*180* ± 20	-	*1990* ± 100	*2050* ± 100	*4* ± 2	-	*(> 513)*
6h @ 490 °C	90 °		-				-	
As-Built	**0°**	161	0.24	1069	1174	15.7	56	382
	45°	140	0.29	991	1144	6.8	56	327
	90°	122	0.35	892	1057	13.8	62	375
6h @ 460°C	**0°**	182	0.31	1908	1971	6.5	22	594
	45°	183	0.30	1850	1939	6.2	18	593
	90°	170	0.33	1803	1907	7.0	19	591
8h @ 460 °C	**0 °**	178	0.33	1951	2006	7.4	24	602
	45 °	178	0.29	1907	1987	7.4	20	590
	90 °	171	0.30	1849	1939	6.9	23	603
12h @ 460 °C	**0°**	177	0.34	1979	2032	6.6	22	610
	45°	180	0.31	1941	2022	6.0	21	607
	90°	171	0.32	1888	1965	5.6	19	610
4h @ 490 °C	**0°**	182	0.33	1961	2004	8.6	33	603
	45°	185	0.31	1895	1963	8.0	28	595
	90°	180	0.32	1875	1928	5.9	24	599
6h @ 490 °C	**0°**	178	0.40	1901	1958	5.9	19	602
	45°	183	0.28	1925	1984	4.4	10	603
	90°	178	0.28	1893	1958	6.1	22	599
8h @ 490 °C	**0°**	183	0.34	1969	2020	8.3	32	608
	45°	184	0.29	1930	1993	7.8	29	606
	90°	180	0.32	1912	1978	4.2	21	615
4h @ 525 °C	**0°**	189	0.33	1811	1882	5.82	35	570
	45°	185	0.29	1811	1878	5.38	30	568
	90°	180	0.3	1797	1885	7.97	23	578
6h @ 525 °C	**0°**	181	0.34	1768	1844	10.4	32	560
	45°	175	0.32	1747	1818	6.9	29	560
	90°	176	0.31	1741	1816	8.5	31	554
8h @ 525 °C	**0°**	179	0.34	1729	1811	10.5	36	552
	45°	181	0.31	1714	1802	9.9	33	558
	90°	181	0.32	1723	1816	10.1	30	557
4h @ 540 °C	**0°**	181	0.34	1700	1769	10.4	37	543
	45°	183	0.32	1697	1778	10.2	38	550
	90°	169	0.30	1656	1744	9.3	33	554
6h @ 540 °C	**0°**	182	0.26	1661	1736	12.4	38	536
	45°	177	0.29	1666	1746	6.7	19	542
	90°	182	0.31	1640	1724	10.5	31	536
8h @ 540 °C	**0°**	182	0.31	1625	1701	11.2	41	525
	45°	177	0.29	1620	1705	11.5	37	534
	90°	174	0.31	1579	1666	10.8	33	531
2h @ 600 °C	**0°**	173	0.32	1326	1440	17.1	49	458
	45°	174	0.29	1312	1425	16.5	53	457
	90°	166	0.29	1290	1405	15.5	51	457
4h @ 600 °C	**0°**	169	0.31	1267	1387	17.2	49	447
	45°	167	0.27	1263	1382	16.7	49	447
	90°	164	0.30	1253	1368	16.0	49	442
6h @ 600 °C	**0°**	166	0.33	1214	1338	17.6	50	430
	45°	173	0.26	1211	1335	17.7	50	432
	90°	157	0.33	1172	1303	14.5	54	432

compared to the other build-orientations. Furthermore, the as-built elastic properties of Elasticity Modulus (*E*) and Poisson ratio (ν) display an inverse relationship with respect to build-orientation. This may be attributed to the alloy's fabrication route.

When analysing the effect of heat-treatment on mechanical anisotropy, Table 4 data indicate that hardness measurements alone are the least effective method to reveal and quantify mechanical anisotropy and helps to explain why similar observations have not been presented in the research literature to-date. A relationship between *hardness* (*H*) and yield strength ($R_{p0.2}$) was devised from the available data, based on similar empirical relationships used for other metals. In particular, the typical linear rule-of-thumb for a broad range of metallic alloys given by Eq. (2) [54] has been used.

$$H \approx 3 \times R_{p0.2} \tag{2}$$

Eq. (2) holds true except in the cases of the as-built and severely overaged material (e.g. samples aged at 600 °C). Moreover, the hardness (H), described as the indenter force divided by the projected area of the indent (in MPa) is given by Eq.3.

$$H = \mathrm{HV}_{30} \times 9.81 m/s^2 \tag{3}$$

Where HV_{30} is the Vickers hardness value. The bar-chart (Fig. 11) reinforces prior anisotropy observations for the as-built and aged alloy across the range of experimental treatments and suggests that a certain anisotropy remains following aging.

As shown for the hardness measurements in Fig. 9, even for the low aging temperature (460 °C) the greatest percentage of the treatment's peak hardness is obtained within the early stages of aging (during underaging). The rate of early-stage hardening is due the populous development of small and coherent first-stage precipitates which shear the

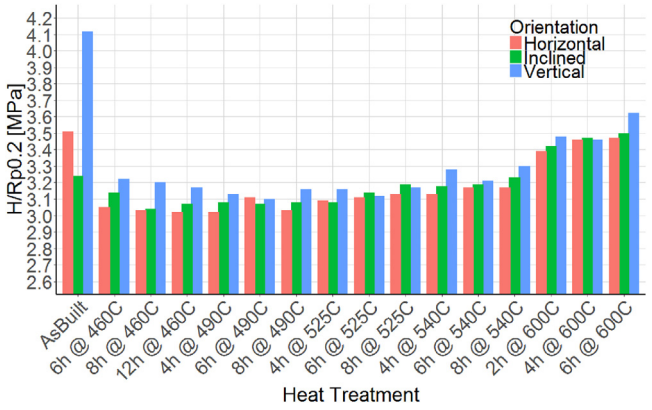

Fig. 11. Ratio of Hardness (H) to Yield Strength for the as-built and heat-treated MS1 examined.

passing dislocations [38]. This lower temperature somewhat regulates early-precipitation diffusion kinetics allowing particles to grow by a greater extent before overaging dominates. For this reason, the greater population of particles at lower treatment temperatures provides an enhanced strengthening effect, however, as previously mentioned, the time taken to achieve peak strength/hardness increases alongside. Despite the narrow temperature window, and harmonious strengthening-relationship between 460 and 490 °C, it takes 4h longer for the former to reach its peak-hardness condition.

As indicated in Table 4, the obtained as-built and aged (6h at 490 °C) mechanical properties agree with EOS published figures with exceptions for the as-built 90° elasticity modulus and yield-strength experimental values which under-perform slightly. As-built test-specimens displayed the largest hardness variation. The mean and standard deviation (SD) with respect to the build orientations was 362HV and 25HV in that order. This relatively large variation was reflected across the full range of as-built mechanical properties, for example: the mean and SD yield strength ($R_{p0.2}$), and total elongation (At), were 984 MPa (with SD = 89 MPa) and 12% (with SD = 4.7%) respectfully. Higher recorded hardness values were observed jointly in specimens aged at 460 °C for 12h; and 490 °C for 8h which measured 609HV (with SD = 4HV), and 609HV (with SD = 5HV) respectively. Highest yield strength was 1936MPa (with SD = 46 MPa) and tensile strength was 2006 MPa (with SD = 36MPa) for the specimens aged at 460 °C for 12h, but there was little mechanical property difference between the 12h at 460 °C and 8h at 490 °C heat-treatments. These optimal strength values were accompanied by a sharp reduction in ductility, evaluated at 5–6% on average.

The aging and stress (σ) - strain (ϵ) curves show clear evidence of overaging when temperatures exceed 490 °C, most noticeably at 600 °C where the alloy is heated into the austenite phase transformation zone. This observed loss of hardness/strength is based on Orowan's mechanism of dispersion hardening, where passing dislocations loop around larger and more dispersed stage-two Fe_2Mo and/or Fe_7Mo_6 precipitates [55,56]. The effectiveness of dislocation hindrance in the overaged specimens is much reduced due to the combined loss of precipitate-lattice coherency, and the increasing sparsity of these blocking particles. Overaged specimens also display increased strain-hardening, corresponding to the wider dispersion of particles whereby the build-up of subsequent gliding dislocation loops heighten the degree of back-stress in the lattice. These overaged AM MS1 properties, not previously reported, may be useful to AM practitioners when good toughness is sought, as indicated by the area under the σ versus ϵ curves.

Further evaluation of plastic anisotropy has been performed via the DIC obtained R-value measurements. The R-value is defined as the true width-to-thickness strain, given by Eq. (4).

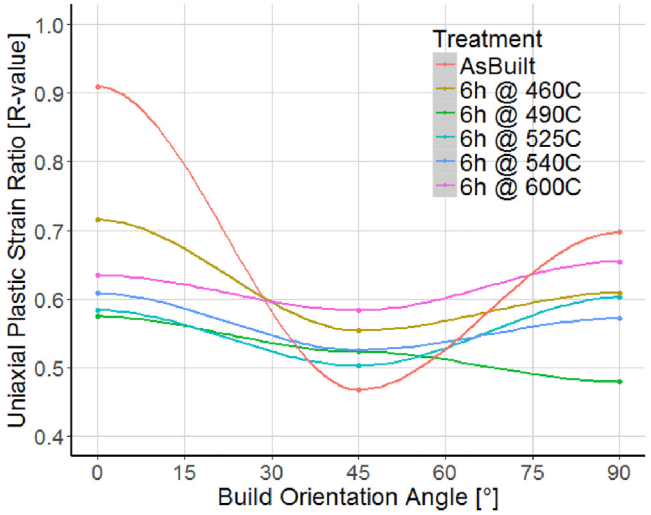

Fig. 12. Plot of R-values versus build orientation angle, evaluated at 1.5% axial strain. The trend patterns for this selection of representative heat-treatments are displayed using local polynomial regression fitting.

$$R \text{ value} = \frac{\varepsilon_w}{\varepsilon_t} \tag{4}$$

The obtained results are shown in Fig. 12, which highlight (i) non-uniform transverse straining since $R_{isotropic} = 1$; and (ii) R-value variation between AM build orientation angles. As with the mechanical properties, a significant reduction in plastic strain anisotropy was observed following the application of aging heat-treatments. The precipitation of nanometric dislocation hindering precipitate particles is exclusively responsible hence. The test-specimens, regardless of their build orientation and heat treatment, consistently displayed a ratio of true width-to-thickness strains (R-values) below unity (< 1) within the alloy's elastic-plastic regime. While these harmonious trends indicate that the plastic-strain behaviour is more-or-less uniform in the Y-Z build plane, they signify greater thinning in specimens' thickness direction, and suggest that the 67° laser scan rotation between layers, and subsequent aging heat-treatment, are not sufficient to suppress anisotropic transverse strain behaviour. Depending on the engineering application, it may therefore be necessary to perform a solubilization treatment step prior to aging which could abolish any fabrication manifested microstructural patterning, achieve a derivative stress relaxation, ensure the dissolution of detrimental phases, and ultimately homogenise the microstructure. However, such circumstances incur additional processing cost, complexity and time, which subtracts from the overall AM maraging steel 300 appeal.

The experimental findings indicate that the AM induced anisotropy cannot be eliminated through application of the 6h at 490 °C heat-treatment. Furthermore, this heat-treatment plan is not optimal for the alloy's strength, ductility, hardness, or anisotropy. To address this issue, mean mechanical property values (with respect to the build orientations) from the complete set of experimental results (as outlined in Table 2) have been used to construct contour surface plots. In particular, bi-variate interpolation of x (aging time), y (aging temperature), and z (response variables: $R_{p0.2}$, R_m, At, HV, and ΔR-values (Eq. (1)) components has been applied to represent a smooth surface of z values at selected points distributed in the x-y plane using the R statistical software package [46,57]. These plots (shown in Fig. 13), may act as a guide for selection of tailored heat-treatments, when specific mechanical properties and anisotropy limits are required for an AM part.

Fig. 13 clearly communicates that the chosen aging parameters correspond to significantly different achievable mechanical properties in DMLS MS1. Remarkable strength and hardness can be installed by underaging the alloy between 460 and 525 °C (see Figs. 13(a), (b), and

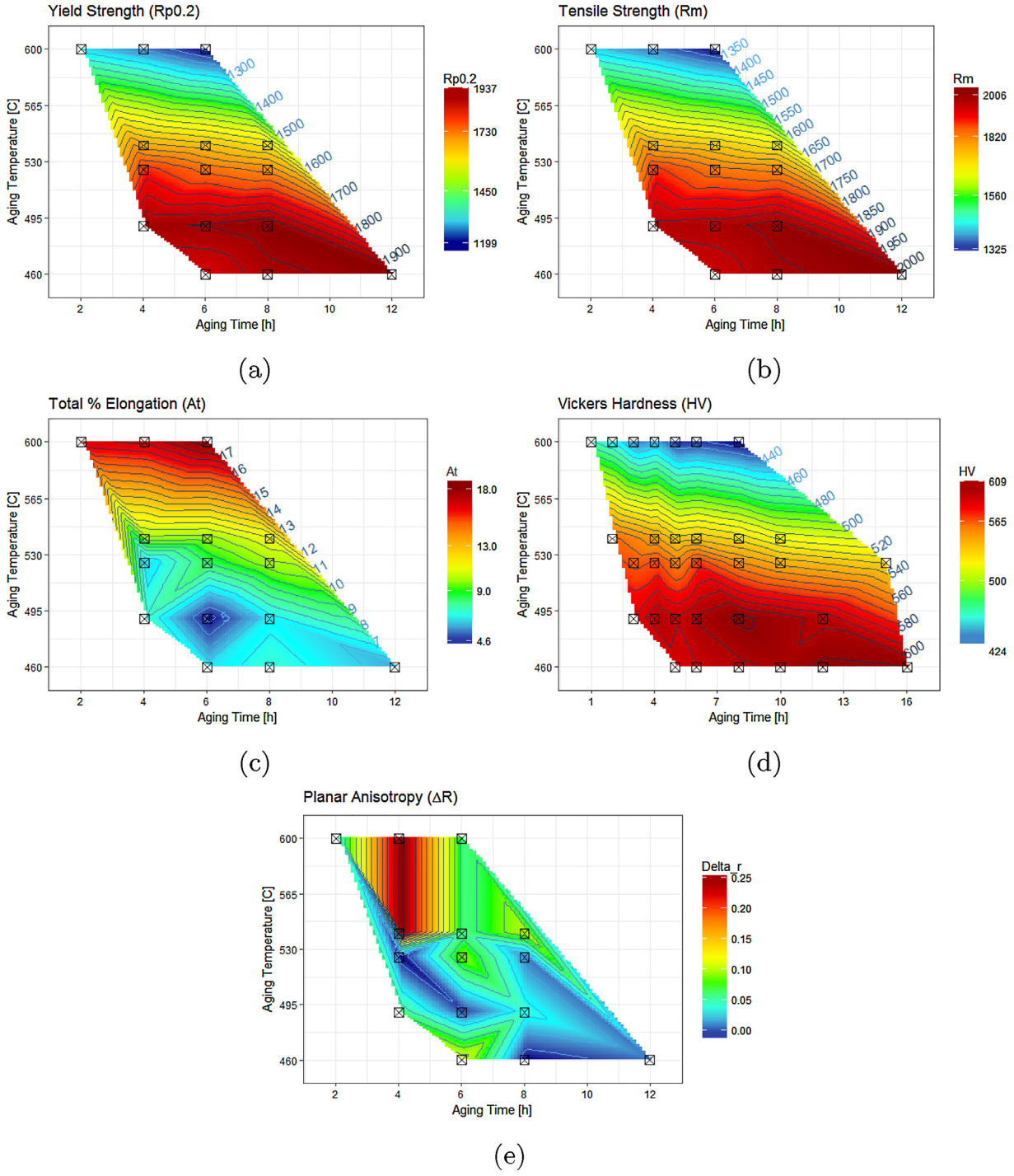

Fig. 13. Interpolated smooth surface contour plots of experimentally determined (marked) AM MS1 properties (a) Yield strength ($R_{p0.2}$); (b) Tensile strength (R_m); (c) Total % Elongation (At); (d) Vickers hardness (HV); and (e) Planar anisotropy (ΔR) evaluated at 1.5% axial strain.

(d)), however, ductility (and toughness) are markedly reduced in this condition (see Fig. 13(c)). When increased ductility is sought, the alloy can be aged at temperatures above 525 °C, though a loss of strength and hardness can be expected as overaging and austenite reversion rapidly take hold. The ΔR contour plot for R-values evaluated at 1.5% axial strain is shown in Fig. 13(e). ΔR, calculated using Eq. (1), represents an overall measure of the variation of R-value in the Y-Z build plane (planar anisotropy) where for an isotropic material: $\Delta R = 0$. For AM materials, non-zero values of ΔR could be an indicator of preferred texture / alignment of the micro-structure due to the laser scanning pattern (especially in the distribution of second phases such as inclusions) / the presence of residual stresses [58]. The contour plot highlights that the range of ΔR variation is low across all treatments (< 0.25 at 1.5% axial strain). Planar anisotropy is minimised in the underaged to peak-aged condition. The hypothesis is that the populous presence of small precipitates effectively conceals non-uniform transverse straining by blocking gliding dislocations in this stiff and brittle condition. Comparatively, a greater degree of planar anisotropy can be observed in the overaged and austenitized material, where a lattice with fewer blocking obstacles, and a higher volume fraction of ductile Fe-γ, sees ΔR deviate from zero.

4. Conclusions

As AM technology continues to mature, more is expected of the functional parts produced, with special attention towards achieving metallurgical soundness by tackling the factors which influence mechanical performance. This study has investigated the effect of three AM build-orientations (0°, 45°, and 90°) on the as-built plastic anisotropy of maraging steel 300 (MS1) parts, fabricated on the commercially available EOS EOSINT M280 machine. This high-strength alloy's performance has been monitored through an array of strengthening heat-treatment plans to identify the combinations of time and temperature which can diminish anisotropy. In doing so, a broad collection of mechanical properties, material characteristics, and plastic anisotropy levels for additively manufactured standard test-specimens have been evaluated and discussed in this novel experimental investigation. The important conclusions are summarized as follows:

1. Considerable anisotropy has been confirmed in as-built MS1;
2. Plastic anisotropy can be diminished significantly through aging heat-treatment, however, a degree of transverse strain anisotropy is likely to remain due to the AM material's fabrication history;
3. The 6h at 490 °C heat treatment plan is not optimal in terms of strength, hardness, ductility and anisotropy properties for the DMLS MS1. A proposition of 8h at 490 °C is offered where optimal design strength ($R_{p0.2}$ > 1900 MPa) is sought, whereas the 8h at 525 °C aging plan offers a good isotropic compromise between design strength ($R_{p0.2}$ > 1700 MPa), and ductility ($A_t \approx$ 10%);
4. Heat-treatment parameters can be tailored to meet strength/ ductility/ anisotropy design requirements by using the obtained mechanical properties contour maps;
5. The as-built and overaged specimens showed higher levels of planar anisotropy compared to that of the underaged and peak-aged condition;
6. Hardness measurements alone are not effective towards quantifying anisotropy in DMLS maraging steel 300.

Acknowledgement

This research project has been jointly funded by the Irish Research Council (IRC), through the Government of Ireland Postgraduate Research Programme, and the Faculty of Science and Engineering of the University of Limerick.

References

[1] J. Davis (Ed.), Alloying: Understanding the Basics, ASM International, OH, USA, 2001ISBN: 978-0-87170-744-4.
[2] A. Hall, C. Slunder, The Metallurgy, Behaviour, and Application of the 18-percent Nickel Maraging Steels, Survey 20000828 057, NASA, 1968. URL: http://www.dtic.mil/dtic/tr/fulltext/u2/a382105.pdf, sP-5051.
[3] M. Stanford, K. Kibble, M. Lindop, D. Mynors, C. Durnall, An investigation into fully melting a maraging steel using direct metal laser sintering (dmls), Special Edition Metal Forming Conference 2008, 79 (2008) 847–852.
[4] F. Tariq, N.R.A.B. Naz, Effect of cyclic aging on mechanical properties and microstructure of maraging steel 250, J. Mater. Eng. Performance 19 (2010) 1005–1014.
[5] L.M. Kleiner, Y.N. Simonov, Structure and properties of low-carbon martensitic steels, Metal Sci. Heat Treatment 41 (1999) 366–368.
[6] E.A. Jägle, Z. Sheng, L. Wu, L. Lu, J. Risse, A. Weisheit, D. Raabe, Precipitation reactions in age-hardenable alloys during laser additive manufacturing, JOM 68 (2016) 943–949.
[7] R. Casati, J. Lemke, A. Tuissi, M. Vedani, Aging behaviour and mechanical performance of 18-ni 300 steel processed by selective laser melting, Metals 6 (2016).
[8] F. Lang, N. Kenyon, WRC Bulletin: Welding of Maraging Steels, Technical Report 159, Welding Research Council, USA, 1971.
[9] Inco, 18 per cent maraging steels, Technical Report 4419, International Nickel Company, 1976.
[10] EOS, Materials for metal additive manufacturing, 2017. URL: https:// www.eos.info/material-m.
[11] EOS, EOS MaragingSteel MS1, Material data sheet EOSINT M280 EOSINT M270, Electro Optical Systems (EOS), 2011. URL: http://ip-saas-eos-cms.s3.amazonaws.com/public/1af123af9a636e61/042696652ecc69142c8518dc772dc113/EOS_MaragingSteel_MS1_en.pdf.
[12] M. Frey, M. Shellabear, L. Thersson, Mechanical Testing of DMLS Parts, White Paper, Electro Optical Systems (EOS), 2015 URL: http://www.fabricadeprototipos.com/links/DMLS/link2_ensaiosmecanicos.pdf.
[13] Renishaw, Maraging steel M300 powder for Additive manufacturing, Data sheet, Renishaw, 2017. URL: http://resources.renishaw.com/en/download.
[14] G. Casalino, S. Campanelli, N. Contuzzi, A. Ludovico, Experimental investigation and statistical optimisation of the selective laser melting process of a maraging steel, Opt Laser Technol. 65 (2015) 151–158.
[15] S.L. Campanelli, N. Contuzzi, A.D. Ludovico, Manufacturing of 18 ni marage 300 steel samples by selective laser melting, Advances in Materials and Processing Technologies, volume 83 of Advanced Materials Research, Trans Tech Publications. doi: 10.4028/www.scientific.net/AMR. 83-86.850, 2010, pp. 850–857.
[16] J. Mutua, S. Nakata, T. Onda, Z. Chen, Optimization of selective laser melting parameters and influence of post heat treatment on microstructure and mechanical properties of maraging steel, Mater. Design 139 (2018) 486–497.
[17] K. Monkova, I. Zetkova, L. Kučerová, M. Zetek, P. Monka, M. Daňa, Study of 3d printing direction and effects of heat treatment on mechanical properties of ms1 maraging steel, Arch. Appl. Mech. (2018) 1–14.
[18] D. Croccolo, M. De Agostinis, S. Fini, G. Olmi, A. Vranic, S. Ciric-Kostic, Influence of the build orientation on the fatigue strength of eos maraging steel produced by additive metal machine, Fatigue Fract. Eng. Mater. Struct. 39 (2016) 637–647.
[19] T. Burkert, A. Fischer, The effects of heat balance on the void formation within marage 300 processed by selective laser melting, in: (Ed.), International Solid Freeform Fabrication Symposium, University of Texas, 2015, pp. 745-757. URL: http://sffsymposium.engr.utexas.edu/sites/default/files/2015/2015-61-Burkert.pdf.
[20] N. Contuzzi, S. Campanelli, G. Casalino, A. Ludovico, Effect of heat treatment on selective laser melted steel parts, in: B. Katalinic (Ed.), Annals of DAAAM for 2010 & Proceedings of the 21st International DAAAM Symposium, 1, DAAAM International. URL: www.daaam.info/Downloads/Pdfs/proceedings/...2010/24802_Symp_1_head.pdf, 2010, pp. 1–2.
[21] K. Kempen, E. Yasa, L. Thijs, J.-P. Kruth, J. Van Humbeeck, Microstructure and mechanical properties of selective laser melted 18ni-300 steel, Phys. Procedia 12 (2011) 255–263 Lasers in Manufacturing 2011 - Proceedings of the Sixth International WLT Conference on Lasers in Manufacturing.
[22] D. Koutney, L. Panteljev, J. Tomes, D. Palousek, Comparison of selective laser melting of 18ni maraging steel by pxl and m2 cusing, MM (Modern Machinery) Science Journal (2016) 1590–1596.
[23] C. Tan, K. Zhou, X. Tong, Y. Huang, J. Jing, W. Ma, F. Li, T. Kuang, Microstructure and mechanical properties of 18ni-300 maraging steel fabricated by selective laser melting, in: 6th International Conference on Advanced Design and Manufacturing Engineering (ICADME 2016), Atlantis Press. URL: http://www.atlantis-press.com/php/download_paper.php?id=25862785, 2016, pp. 404–410.
[24] J. Sedlak, D. Rican, M. Piska, L. Rozkosny, Study of materials produced by powder metallurgy using classical and modern additive laser technology, Procedia Eng. 100 (2015) 1232–1241 Part of Special issue 25th DAAAM International Symposium on Intelligent Manufacturing and Automation, 2014.
[25] T. Becker, D. Dimitrov, The achievable mechanical properties of slm produced maraging steel 300 components, Rapid Prototyping J. 22 (2016) 487–494.
[26] R. Casati, J. Lemke, M. Vedani, Microstructural and mechanical properties of as built, solution treated and aged 18 ni (300 grade) maraging steel produced by selective laser melting, La Metallurgia Italiana (2017) 11–20.
[27] J. Suryawanshi, K. Prashanth, U. Ramamurty, Tensile, fracture, and fatigue crack growth properties of a 3d printed maraging steel through selective laser melting, J. Alloys Compd. 725 (2017) 355–364.
[28] S. Yin, C. Chen, X. Yan, X. Feng, R. Jenkins, P. O'Reilly, M. Liu, H. Li, R. Lupoi, The influence of aging temperature and aging time on the mechanical and tribological properties of selective laser melted maraging 18ni-300 steel, Addit. Manuf. 22 (2018) 592–600.
[29] Y. Bai, Y. Yang, D. Wang, M. Zhang, Influence mechanism of parameters process and mechanical properties evolution mechanism of maraging steel 300 by selective laser melting, Mater. Sci. Eng. A 703 (2017) 116–123.
[30] C. Tan, K. Zhou, W. Ma, P. Zhang, M. Liu, T. Kuang, Microstructural evolution, nanoprecipitation behavior and mechanical properties of selective laser melted high-performance grade 300 maraging steel, Mater. Design 134 (2017) 23–34.
[31] l. Kucerova, I. Zetkova, Metallography of 3d printed 1.2709 tool steel, Manuf. Technol. 16 (2016) 140–144.
[32] N. Takata, R. Nishida, A. Suzuki, M. Kobashi, M. Kato, Crystallographic features of microstructure in maraging steel fabricated by selective laser melting, Metals 8 (2018) Special Issue Additive Manufacturing of Ferrous Materials.
[33] E. Jägle, P. Choi, J. Van Humbeeck, D. Raabe, Precipitation and austenite reversion behavior of a maraging steel produced by selective laser melting, J. Mater. Res. 29 (2014) 2072–2079.
[34] D. Bourdil , Microstructure and Mechanical Properties of Maraging Steel 300 After Selective Laser Melting 2010; URL: https://sffsymposium.engr.utexas.edu/Manuscripts/2010/2010-32-Yasa.pdf.
[35] EOS, EOSINT M 280, Technical Description, Electro Optical Systems (GmbH), 2010. URL: https://webbuilder5.asiannet.com/ftp/2684/TD_M280_en_2011-03-29.pdf.
[36] ASTM, ASTME8/E8M-16a: Standard Test Methods for Tension Testing of Metallic Materials, Test Standard, ASTM, 2016. URL: http://www.astm.org/cgi-bin/resolver.cgi?E8E8M-16a. doi: 10.1520/E0008_E0008M-16A.
[37] F. Pfefferkorn, J. Wielhammer, Open and Flexible:, White Paper, EOS (gmbh), 2013. URL: https://cdn3.scrvt.com/eos/public/7e99ba072eca9ad8/294354957693f78ddb4787d3959e7057/ppm_whitepaper.pdf.
[38] W. Sha, Z. Guo, Maraging Steels, Modelling of Microstructure, Properties and Applications, Woodhead Publishing, Cambridge UK, 2009 ISBN: 978-1-84569-

686-3.
[39] EOS, Machine and software parameters EOSINT M 280, Parameter Sheet, Electro Optical Systems (EOS), 2015. Made available to EOSINT M280 machine owners by request to EOS (not published).
[40] ASTM, ASTMB962-17: Standard Test Methods for Density of Compacted or Sintered Powder Metallurgy (PM) Products Using Archimedes' Principle, Test Standard, ASTM, 2017.
[41] LaVision, StrainMaster: Product Manual for DaVis 8.3, Manual 1003017, LaVision, DE, 2017. Page total: 122.
[42] LaVision, Full field strain measurement, 2014. URL: http://www.lavision.de/en/applications/materials-testing/stereo-dic/index.php.
[43] ASTM, ASTME132-04: Standard Test Method for Poisson's Ratio at Room Temperature, Test Standard, ASTM, 2004. URL: http://www.astm.org/cgi-bin/resolver.cgi?E132-04. doi: 10.1520/E0132-04.
[44] ASTM, ASTME517-18: Standard Test Method for Plastic Strain Ratio r for Sheet Metal, Test Standard, ASTM, 2018. URL: https://www.astm.org/Standards/E517.htm. doi: 10.1520/E0517-18.
[45] ASTM, ASTME92-17: Standard Test Methods for Vickers Hardness and Knoop Hardness of Metallic Materials, Test Standard, ASTM, 2017. URL: https://www.astm.org/Standards/E92.htm.
[46] R Core Team, R: A Language and Environment for Statistical Computing, Technical Report, R Foundation for Statistical Computing, Vienna, Austria, 2014. URL: http://www.R-project.org/.
[47] E. Jägle, Z. Sheng, P. Kurnsteiner, S. Ocylok, A. Weisheit, D. Raabe, Comparison of maraging steel micro- and nanostructure produced conventionally and by laser additive manufacturing, Materials 10 (2017).
[48] T. Niendorf, S. Leuders, A. Riemer, H.A. Richard, T. Tröster, D. Schwarze, Highly anisotropic steel processed by selective laser melting, Metall. Mater. Trans. B 44 (2013) 794–796.
[49] T. Etter, K. Kunze, F. Geiger, H. Meidani, Reduction in mechanical anisotropy through high temperature heat treatment of hastelloy x processed by selective laser melting (slm), IOP Conf. Series: Mater. Sci. Eng. 82 (2015) 012097.
[50] K. Kunze, T. Etter, J. Grässlin, V. Shklover, Texture, anisotropy in microstructure and mechanical properties of in738lc alloy processed by selective laser melting (slm), Mater. Sci. Eng.: A 620 (2015) 213–222.
[51] V. Popovich, E. Borisov, A. Popovich, V. Sufiiarov, D. Masaylo, L. Alzina, Functionally graded inconel 718 processed by additive manufacturing: Crystallographic texture, anisotropy of microstructure and mechanical properties, Mater. Design 114 (2017) 441–449.
[52] S. Morito, H. Tanaka, R. Konishi, T. Furuhara, T. Maki, The morphology and crystallography of lath martensite in fe-c alloys, Acta Mater. 51 (2003) 1789–1799.
[53] ASM International, ASM Handbook Volume 4: Heat Treating, volume 4, ASM International, OH, USA, 1991.
[54] M. Ashby, D. Jones, Engineering Materials 2: An Introduction to Microstructures, Processing and Design, Butterworth-Heinemann, New York, USA, 2005 ISBN: 9780080468631.
[55] W. Smith, J. Hashemi, Foundations of Materials Science and Engineering, 3rd ed., McGraw-Hill, New York USA, 2004 ISBN 0-07-240233-4.
[56] G. Dieter, Mechanical Metallurgy, McGraw-Hill, New York USA, 1961.
[57] H. Akima, A. Gebhardt, akima: Interpolation of Irregularly and Regularly Spaced Data, (2016) URL: https://CRAN.R-project.org/package=akima, r package version 0.6-2.
[58] B. Hutchinson, Critical assessment 16: Anisotropy in metals, Mater. Sci. Technol. 31 (2015) 1393–1401.